

Exchange-Correlation Potentials and Energy Densities through Orbital Averaging and Aufbau Integration

Vaibhav Khanna,[†] Bikash Kanungo,[‡] Jeffrey Hatch,[†] Joshua Kammeraad,[†] and
Paul M. Zimmerman^{*,†}

[†]*Department of Chemistry, University of Michigan, Ann Arbor, Michigan 48109, United States*

[‡]*Department of Mechanical Engineering, University of Michigan, Ann Arbor, Michigan 48109, United States*

E-mail: paulzim@umich.edu

Abstract

Exchange-correlation potentials (v_{xc}) and energy densities (e_{xc}) are derived for integer and fractional electron counts using an orbital-averaged (OA) Kohn-Sham (KS) inversion procedure. The reference densities for inversion come from full configuration interaction (FCI) in a Slater orbital basis. The OA potentials accurately capture key features of v_{xc} , including the asymptotic $-1/r$ decay and the step discontinuity associated with integer electron transitions for the series of atoms He through Ne. Exchange-correlation energy densities e_{xc} are produced through an aufbau path integral. The energy densities reach good agreement with total E_{xc} values. By providing FCI-derived KS quantities— v_{xc} , e_{xc} , and step contributions—this workflow can be instrumental in the development of improved XC functionals that bridge wavefunction-level accuracy with the computational efficiency of density functional theory.

Introduction

Density functional theory (DFT) is central to modern first principles studies of molecules and materials.¹ DFT strikes a balance between accuracy, generality, and computational feasibility that is not attained by related methods, and therefore can be usefully applied to simulations of molecules and materials containing many electrons.²⁻⁷ Most practical DFT methods build upon the Kohn-Sham (KS) formalism,⁸ which transforms the many-electron problem into a set of single-particle equations. The electrons, instead of interacting with one another as in wave function theory (WFT), formally experience only an effective potential. Describing the KS potential is therefore key to unlocking the full capabilities of DFT.

The KS equations are written as:

$$\left(-\frac{1}{2}\nabla^2 + v_{\text{ext}}(\mathbf{r}) + v_H(\mathbf{r}) + v_{xc}(\mathbf{r})\right)\phi_i(\mathbf{r}) = \epsilon_i\phi_i(\mathbf{r}), \quad (1)$$

where $v_{\text{ext}}(\mathbf{r})$ is the external potential, $v_H(\mathbf{r})$ is the Hartree potential, and $v_{xc}(\mathbf{r})$ is the quantum, or exchange-correlation (XC), potential. The KS eigenstates, $\phi_i(\mathbf{r})$, map onto the electron density $\rho_{\text{KS}}(\mathbf{r})$, via $\rho_{\text{KS}}(\mathbf{r}) = \sum_{i=1}^N n_i |\phi_i(\mathbf{r})|^2$. Performing KS computations requires an approximate exchange-correlation functional, $E_{xc}[\rho]$, which in turn gives v_{xc} through

$$v_{xc}(\mathbf{r}) = \frac{\delta E_{xc}[\rho]}{\delta \rho(\mathbf{r})}, \quad (2)$$

The exchange-correlation potential, v_{xc} , is a critical element in DFT because the other pieces of the KS potential can be described classically. The exact forms of E_{xc} and v_{xc} are unknown.⁹

One way to build understanding of XC potentials is through inverse Kohn-Sham (invKS) theory. To inform the modeling of E_{xc} , invKS constructs v_{xc} from given electron densities, particularly those from ab initio WFT.¹⁰⁻¹⁶ invKS allows investigation of the properties of exact XC potentials that can serve as a benchmark for approximate functionals.¹⁷⁻¹⁹ In the particular case of 1- or 2-electron systems, the exact exchange-correlation potential $v_{xc}(\mathbf{r})$

can be derived analytically from the electron density:

$$v_{xc}(\mathbf{r}) = \frac{\nabla^2 \rho(\mathbf{r})}{4\rho(\mathbf{r})} - \frac{|\nabla \rho(\mathbf{r})|^2}{8\rho(\mathbf{r})^2} - v_{ext}(\mathbf{r}) - v_H(\mathbf{r}) + \epsilon, \quad (3)$$

This expression provides a non-iterative means to compute $v_{xc}(\mathbf{r})$, though it formally requires exact densities to produce meaningful results.²⁰

The invKS problem is ill-posed in incomplete bases, which can lead to non-unique solutions and unphysical potentials.^{21–25} Finite basis sets like GTOs struggle to accurately represent density near nuclei and at large distances, often resulting in oscillatory potentials.^{18,19,25} This sensitivity to numerical artifacts and basis set limitations makes inversion challenging.^{26,27} These limitations have led to the development of inversion methods that either bypass the constraints of Gaussian-type basis sets or use systematically complete basis representations. Among these, the KZG constrained optimization method introduced by Kanungo et al.^{28,29} employs a finite-element basis that achieves systematic convergence, thereby providing accurate XC potentials. This method formulates the invKS problem as an optimization task, minimizing the difference between the KS density and a target density. The method has demonstrated success in providing stable XC potentials for a variety of molecular systems.³⁰ In addition, the multiresolution analysis (MRA) method developed by Stückrath and Bischoff³¹ achieves similar goals through a systematic approach to the complete basis set limit.

The Ryabinkin-Kohut-Staroverov (RKS) method provides an alternative to inversion that is applicable to finite basis set computations. Rather than relying on fitting the density, v_{xc} is iteratively constructed using the KS equations and quantities derived from the two-electron reduced density matrix (2-RDM) of WFT.^{32–34} The RKS method balances local energy contributions in KS theory and WFT to yield XC potentials that are free from artifacts of incomplete basis sets. While the RKS method is not designed to reproduce the exact density, XC potentials from RKS are much less sensitive to basis set than those from invKS methods. Our group recently extended the RKS method to employ Slater basis functions,³⁵

which capture the nuclear cusp condition and exponential decay of electron density. The SlaterRKS method proved effective in computing v_{xc} for strongly correlated systems, such as stretched H_2 and CH_2 , using FCI densities as input.³⁵

An earlier strategy for constructing v_{xc} , first explored by Baerends and co-workers,^{36,37} was later evolved into a practical inversion method by Kananenka et al.³⁸ In particular, given a set of KS orbitals, $\{\phi_i(\mathbf{r})\}$, the orbital-averaged v_{xc} is expressed as:

$$v_{xc}(\mathbf{r}) = \frac{\sum_{i=1}^N (\epsilon_i |\phi_i(\mathbf{r})|^2 + \frac{1}{2} \phi_i^*(\mathbf{r}) \nabla^2 \phi_i(\mathbf{r}))}{\rho(\mathbf{r})} - v_{\text{ext}}(\mathbf{r}) - v_H(\mathbf{r}) \quad (4)$$

Kananenka showed that this approach is applicable to existing density functionals, where $\{\phi_i(\mathbf{r})\}$ and ϵ_i are available. On the other hand, if exact KS orbitals were available—for instance those that reproduce a correlated wavefunction density—orbital averaged potentials could also be formed to represent v_{xc} .

Recent work by Rask et al. outlined a way to produce KS orbitals directly from WFT densities within a Slater basis, providing KS eigenvectors without knowledge of the XC potential or solving the KS equations.³⁹ This method minimizes the difference between the KS and FCI densities, and applies Levy’s variational principle to minimize the KS kinetic energy.⁴⁰ The procedure balances density fitting with kinetic energy minimization, controlled by a mixing parameter λ , which plays a critical role in determining the quality of the resulting KS orbitals. Smaller λ values prioritize close agreement with the FCI density, while larger λ values favor reduced kinetic energy. As with the RKS method, larger basis sets produce more accurate densities as well as potentials.

Our approach builds on these methods by using the KS orbitals directly for the inversion process. Leveraging the CI-derived KS orbitals from Rask’s procedure within an orbital-averaged inversion framework, we compute v_{xc} efficiently and accurately for He through Ne, for a wide range of electron counts, including fractional charges. By employing a sizable Slater basis, this method reliably captures key features like nuclear cusps and exponential decay. We further extend these capabilities by computing spatially resolved exchange-

correlation energy densities e_{xc} from v_{xc} using the line integral method.⁴¹ The line integral formulation requires knowledge of v_{xc} along a well-defined path. Existing inversion approaches like SlaterRKS³⁵ and KZG²⁸⁻³⁰ have not been extended to compute energy densities, as they become prohibitively expensive when performing inversion along an entire path to determine e_{xc} . The herein proposed workflow can systematically obtain e_{xc} from CI-derived orbital-averaged XC potentials along paths described by CI wavefunctions. Having access to accurate e_{xc} from wavefunction theory will allow for improved training and refinement of XC functionals.

Methods and Theory

Obtaining KS Orbitals from FCI Densities

In this work, KS orbitals are derived from Full Configuration Interaction (FCI) electron densities using Rask and coworker’s optimization procedure.³⁹ This procedure minimizes the difference between the KS and FCI densities along with the kinetic energy. The objective function is expressed as

$$\Phi^{\text{KS}} = \arg \min \left(\int |\rho_{\text{WF}}(\mathbf{r}) - \rho_{\text{KS}}(\mathbf{r})|^2 dr + \lambda \langle \Phi^{\text{KS}} | \hat{T} | \Phi^{\text{KS}} \rangle \right), \quad (5)$$

where $\rho_{\text{WF}}(\mathbf{r})$ is the FCI density, $\rho_{\text{KS}}(\mathbf{r})$ is the KS density, and $\langle \Phi^{\text{KS}} | \hat{T} | \Phi^{\text{KS}} \rangle$ is the kinetic energy of the KS system. The parameter λ controls the balance between density fitting and kinetic energy minimization.

The KS electron density is constructed from the KS orbitals as:

$$\rho_{\text{KS}}(\mathbf{r}) = \sum_{i=1}^N n_i |\phi_i(\mathbf{r})|^2, \quad (6)$$

where N is the number of occupied spin orbitals. The KS orbitals are expanded in a finite basis set $\{\chi_\mu(\mathbf{r})\}$:

$$\phi_i(\mathbf{r}) = \sum_{\mu=1}^M C_{\mu i} \chi_{\mu}(\mathbf{r}), \quad (7)$$

where $C_{\mu i}$ are the coefficients of the basis expansion. The KS density is then:

$$\rho_{\text{KS}}(\mathbf{r}) = \sum_{i=1}^N n_i \left(\sum_{\mu=1}^M C_{\mu i} \chi_{\mu}(\mathbf{r}) \right)^2. \quad (8)$$

The KS orbitals must satisfy the orthogonality condition $C^T S C = I$, where $S_{\mu\nu}$ is the overlap matrix. The optimization minimizes the objective function using unitary rotations of the molecular orbitals. See Ref [39] for further details.

Orbital-Averaged Exchange-Correlation Potential v_{xc}

The exchange-correlation potential $v_{xc}(\mathbf{r})$ is computed from the Kohn-Sham eigenvalues ϵ_i and orbitals $\phi_i(\mathbf{r})$ using the orbital-averaged inversion framework.³⁶⁻³⁸ Starting with the Kohn-Sham equation for orbital $\phi_i(\mathbf{r})$:

$$\left[-\frac{1}{2} \nabla^2 + v_{\text{ext}}(\mathbf{r}) + v_H(\mathbf{r}) + v_{xc}(\mathbf{r}) \right] \phi_i(\mathbf{r}) = \epsilon_i \phi_i(\mathbf{r}) \quad (9)$$

Multiplying both sides by $n_i \phi_i^*(\mathbf{r})$, where n_i is the occupation number of the orbital:

$$n_i \phi_i^*(\mathbf{r}) \left[-\frac{1}{2} \nabla^2 + v_{\text{ext}}(\mathbf{r}) + v_H(\mathbf{r}) + v_{xc}(\mathbf{r}) \right] \phi_i(\mathbf{r}) = n_i \epsilon_i |\phi_i(\mathbf{r})|^2 \quad (10)$$

Summing over all orbitals:

$$\sum_{i=1}^N n_i \phi_i^*(\mathbf{r}) \left[-\frac{1}{2} \nabla^2 + v_{\text{ext}}(\mathbf{r}) + v_H(\mathbf{r}) + v_{xc}(\mathbf{r}) \right] \phi_i(\mathbf{r}) = \sum_{i=1}^N n_i \epsilon_i |\phi_i(\mathbf{r})|^2 \quad (11)$$

The total electron density is:

$$\rho(\mathbf{r}) = \sum_{i=1}^N n_i |\phi_i(\mathbf{r})|^2 \quad (12)$$

Dividing by ρ and rearranging for $v_{xc}(\mathbf{r})$:

$$v_{xc}(\mathbf{r}) = \frac{\sum_{i=1}^N n_i (\epsilon_i |\phi_i(\mathbf{r})|^2 + \frac{1}{2} \phi_i^*(\mathbf{r}) \nabla^2 \phi_i(\mathbf{r}))}{\rho(\mathbf{r})} - v_{\text{ext}}(\mathbf{r}) - v_H(\mathbf{r}) \quad (13)$$

This gives the orbital-averaged exchange-correlation potential. The division by $\rho(\mathbf{r})$ avoids singularities in the potential that would arise from dividing by individual KS orbitals, which may contain nodes. Since n_i can take fractional values, this framework is adaptable for systems with fractional electron counts.

Computing Eigenvalues ϵ_j

Because the KS orbitals are derived directly from a WFT density, their corresponding eigenvalues are initially unknown. To compute these eigenvalues, ϵ_j , we project the KS equation onto virtual orbitals ϕ_a , and substitute the orbital-averaged expression for the exchange-correlation potential $v_{xc}(\mathbf{r})$.

We project the Kohn-Sham equation for the occupied orbital, equation 9, onto a virtual orbital ϕ_a , multiplying both sides by $\phi_a^*(\mathbf{r})$ and integrating over all space:

$$\int \phi_a^*(\mathbf{r}) \left[-\frac{1}{2} \nabla^2 + v_{\text{ext}}(\mathbf{r}) + v_H(\mathbf{r}) + v_{xc}(\mathbf{r}) \right] \phi_i(\mathbf{r}) d\mathbf{r} = \epsilon_i \delta_{ai}. \quad (14)$$

Next, we substitute the orbital-averaged expression for $v_{xc}(\mathbf{r})$:

$$v_{xc}(\mathbf{r}) = \frac{\sum_{j=1}^N n_j (\epsilon_j |\phi_j(\mathbf{r})|^2 + \frac{1}{2} \phi_j^*(\mathbf{r}) \nabla^2 \phi_j(\mathbf{r}))}{\rho(\mathbf{r})} - v_{\text{ext}}(\mathbf{r}) - v_H(\mathbf{r}), \quad (15)$$

which leads to the following integral:

$$\int \phi_a^*(\mathbf{r}) \left[-\frac{1}{2} \nabla^2 + \frac{\sum_{j=1}^N n_j (\epsilon_j |\phi_j(\mathbf{r})|^2 + \frac{1}{2} \phi_j^*(\mathbf{r}) \nabla^2 \phi_j(\mathbf{r}))}{\rho(\mathbf{r})} \right] \phi_i(\mathbf{r}) d\mathbf{r} = \epsilon_i \delta_{ai}. \quad (16)$$

On the right-hand side, the Kronecker delta δ_{ai} evaluates to zero since a and i are from

different sets (virtual and occupied, respectively). Therefore, the right-hand side is zero for $a \neq i$, and the equation reduces to solving for the eigenvalues ϵ_j by minimizing the residual.

To find the eigenvalues ϵ_j , we construct the following linear system for the matrix elements B_{iaj} :

$$\sum_j B_{iaj} E_j = R_{ia} \quad (17)$$

where B_{iaj} are the matrix elements from the left-hand side, $E = \{\epsilon_1, \epsilon_2, \dots, \epsilon_N\}$ are the eigenvalues, and R_{ia} is the residual. The goal is to minimize the magnitude of the residual $|R|$ to solve for the eigenvalues ϵ_j .

Using the generalized inverse, the solution to this system is:

$$E = (B^T B)^{-1} B^T R, \quad (18)$$

which minimizes the magnitude of the residual $|R|$ in the least-squares sense.

Furthermore, on projecting the KS equation onto the HOMO,

$$\int \phi_{HOMO}^*(\mathbf{r}) \left[-\frac{1}{2} \nabla^2 + \frac{\sum_{j=1}^N n_j (\epsilon_j |\phi_j(\mathbf{r})|^2 + \frac{1}{2} \phi_j^*(\mathbf{r}) \nabla^2 \phi_j(\mathbf{r}))}{\rho(\mathbf{r})} \right] \phi_{HOMO}(\mathbf{r}) d\mathbf{r} = \epsilon_{HOMO} \quad (19)$$

Here ϵ_{HOMO} is set to be equal to $-I$, (the ionization energy), to ensure that the exchange-correlation potential decays as $-1/r$ at large distances.⁴²⁻⁴⁴ This additional equation is included in the linear system of equations and solved in the same step as equation 18.

By solving the matrix equation 17, we can compute the eigenvalues ϵ_j which, along with CI-derived KS orbitals ϕ_j , fully determine the orbital-averaged exchange-correlation potential $v_{xc}(\mathbf{r})$, via equation 13.

With this workflow, we can compute exchange-correlation potentials directly from CI electron densities, including those associated with non-integer electron counts. For a system with $N_e - \delta$ electrons, the electron density is represented as a linear combination of the

densities for the $N_e - 1$ and N_e electron systems:

$$\rho_{N_e-\delta}^{WF} = (1 - \delta)\rho_{N_e-1}^{WF} + \delta\rho_{N_e}^{WF}, \quad (20)$$

where $\delta \in (0, 1)$. The non-integer electron count δ determines the orbital occupation numbers n_i 's by interpolating between the occupations in the $N_e - 1$ and N_e electron systems. Specifically, an ensemble approach is used, where degenerate p orbitals have equal occupancy. For example, Table 1 illustrates the occupations for a system with $N_e = 5$, $N_e - \delta = 5 - \delta$, and $N_e - 1 = 4$ electrons, showing the interpolation process for determining n_i . The p -electrons are therefore evenly distributed among the p_x , p_y , and p_z orbitals, maintaining spherical symmetry. This choice is neither unique nor necessary, but simplifies the analysis of the atomic systems of this article.

Table 1: Orbital occupations for 5, 5 - δ , where $\delta \in (0,1)$, and 4 electron systems.

	1s	2s	$2p_x$	$2p_y$	$2p_z$
Orbital occupations for $N_e = 5$	2	2	$\frac{1}{3}$	$\frac{1}{3}$	$\frac{1}{3}$
Orbital occupations for $N_e - \delta = 5 - \delta$	2	2	$\frac{1-\delta}{3}$	$\frac{1-\delta}{3}$	$\frac{1-\delta}{3}$
Orbital occupations for $N_e - 1 = 4$	2	2	0	0	0

Transition Between v_{xc} and $v_{xc,\text{Slater}}^{\text{WF}}$

When $\rho(\mathbf{r})$ vanishes at large radial distances from nuclei, the orbital-averaged $v_{xc}(\mathbf{r})$, derived through division by $\rho(\mathbf{r})$, may become numerically unstable. However, it is known that at large r , the exchange-correlation potential v_{xc} and the Slater exchange-correlation potential $v_{xc,\text{Slater}}^{\text{WF}}$ are expected to be identical.^{32,33,35} Hence, a smooth transition is introduced between v_{xc} and $v_{xc,\text{Slater}}^{\text{WF}}$ using the formulation described by Tribedi et al.:³⁵

$$v_{xc}(\mathbf{r}) = F(\mathbf{r})v_{xc}(\mathbf{r}) + (1 - F(\mathbf{r}))v_{xc,\text{Slater}}^{\text{WF}}(\mathbf{r}), \quad (21)$$

where $F(\mathbf{r})$ is defined as:

$$F(\mathbf{r}) = \frac{\rho(\mathbf{r})}{\rho(\mathbf{r}) + \theta}, \quad (22)$$

θ is set to $\theta = 10^{-5}$, to ensure numerical stability.

The Slater potential $v_{xc,\text{Slater}}^{\text{WF}}$ is defined as:

$$v_{xc,\text{Slater}}^{\text{WF}}(\mathbf{r}) = \int \frac{\rho_{xc}^{\text{WF}}(\mathbf{r}, \mathbf{r}_2)}{|\mathbf{r} - \mathbf{r}_2|} d\mathbf{r}_2, \quad (23)$$

where $\rho_{xc}^{\text{WF}}(\mathbf{r}, \mathbf{r}_2)$ is the exchange-correlation hole density, derived from:

$$\Gamma(\mathbf{r}, \mathbf{r}_2; \mathbf{r}, \mathbf{r}_2) = \frac{1}{2} \rho^{\text{WF}}(\mathbf{r}) [\rho^{\text{WF}}(\mathbf{r}_2) + \rho_{XC}^{\text{WF}}(\mathbf{r}, \mathbf{r}_2)]. \quad (24)$$

Here, $\Gamma(\mathbf{r}, \mathbf{r}_2; \mathbf{r}, \mathbf{r}_2)$ is the two-electron reduced density matrix (2-RDM) in coordinate representation.

Line Integration for Energy Densities

Per the general form of the van Leeuwen-Baerends line integral, for an arbitrary path connecting densities ρ_A and ρ_B :

$$E_{xc}[\rho_B] - E_{xc}[\rho_A] = \int_A^B dt \int d\mathbf{r} v_{xc}([\rho_t]; \mathbf{r}) \frac{\partial \rho_t(\mathbf{r})}{\partial t}, \quad (25)$$

where ρ_t is the parametrized density path, evolving from a density ρ_A to ρ_B .^{45,46} Repeated line integrals can in principle connect any density to any other density (or zero density), provided $v_{xc}(\mathbf{r})$ is known for the entire path.

The line integral framework therefore provides considerable flexibility in the choice of the density path ρ_t . Common paths include:

$$\rho_q(\mathbf{r}) = q\rho(\mathbf{r}), \quad \rho_\lambda(\mathbf{r}) = \lambda^3\rho(\lambda\mathbf{r}), \quad \rho_\zeta(\mathbf{r}) = \zeta^2\rho(\zeta^{1/3}\mathbf{r}),$$

where q , λ , and ζ serve as scaling parameters. Each scaling path offers distinct transformations. For instance, from $\lambda = 0$ to $\lambda = 1$, the λ -scaling path preserves the total electron number, while the q -scaling path uniformly scales the density and can be convenient for practical calculations.⁴⁶

In this work, q -scaling is applied piecewise between integer electron counts. Specifically, for a system with N_e electrons, the q -aufbau path over the interval $m - 1 \rightarrow m$, with $m = 1, 2, \dots, N_e$, is defined as:

$$\rho_q(\mathbf{r}) = \rho_{m-1}(\mathbf{r}) + q\Delta\rho_m(\mathbf{r}), \text{ where } \Delta\rho_m(\mathbf{r}) = \rho_m(\mathbf{r}) - \rho_{m-1}(\mathbf{r})$$

and its derivative with respect to q is:

$$\frac{\partial\rho_q(\mathbf{r})}{\partial q} = \Delta\rho_m(\mathbf{r}).$$

Substituting into the line integral formulation,

$$E_{xc}[\rho_m] - E_{xc}[\rho_{m-1}] = \int d\mathbf{r} \int_0^1 v_{xc}([\rho_q]; \mathbf{r}) \Delta\rho_m(\mathbf{r}) dq,$$

we arrive at an integral that connects pairs of integer electron densities and gives their contribution to E_{xc} . The total exchange-correlation energy can be obtained by repeated integration from 0 to N_e electrons.

This line integral also provides a way to extract a spatially resolved exchange-correlation energy density, e_{xc} , along the chosen path.⁴¹ This expression reveals that the term $\int_0^1 v_{xc}([\rho_q]; \mathbf{r}) \Delta\rho_m(\mathbf{r}) dq$ serves as an exchange-correlation energy density:

$$e_{xc}^{m-1 \rightarrow m}([\rho_q]; \mathbf{r}) = \int_0^1 v_{xc}([\rho_q]; \mathbf{r}) \Delta\rho_m(\mathbf{r}) dq,$$

The total energy density is given as:

$$e_{xc}([\rho]; \mathbf{r}) = \sum_{m=1}^{N_e} e_{xc}^{m-1 \rightarrow m}([\rho_q]; \mathbf{r})$$

such that

$$E_{xc}[\rho] = \int e_{xc}([\rho]; \mathbf{r}) d\mathbf{r}$$

This work computes exchange-correlation energy densities using orbital-averaged exchange-correlation potentials and the q-aufbau density path. The gauge of the energy density e_{xc} in our approach is determined by this choice of path. While other paths, and thus other gauges, are in principle available, the stepwise q-aufbau path is convenient when $\rho^{WF}(\mathbf{r})$ is derived from FCI computations.

Capturing the Step Basis Contribution to v_{xc}

As the electron number changes from $N_e - \delta$ to $N_e + \delta$ with δ being a small number, the exact exchange-correlation potential uniformly shifts to reflect the change in integer electron count.^{47,48} It is possible to isolate the uniform shift when computing $v_{xc}(\mathbf{r})$, i.e., the contribution to the potential that is constant throughout space. This can be done by introduction of a "step basis" in the inversion process of equation 13.

To isolate this step basis contribution, we define a set of basis functions b_i 's:

$$b_i(\mathbf{r}) = \frac{n_i |\phi_i(\mathbf{r})|^2}{\sum_{j=1}^N n_j |\phi_j(\mathbf{r})|^2}$$

where due to normalization of the total electron density, we have

$$\sum_{i=1}^N \int b_i(\mathbf{r}) d\mathbf{r} = 1.$$

The basis set $\{b_1, b_2, \dots, b_N\}$ is then transformed into $\{1, b'_2, \dots, b'_N\}$ for step basis contribution extraction. In this transformed basis, the orbital averaged exchange-correlation potential from equation 13 is written as:

$$v_{xc}(r) = \epsilon'_1 + \sum_{i=2}^N b'_i \epsilon'_i + \frac{1}{\rho(\mathbf{r})} \sum_{i=1}^N n_i \left(\frac{1}{2} \phi_i^*(\mathbf{r}) \nabla^2 \phi_i(\mathbf{r}) \right) - v_{\text{ext}}(\mathbf{r}) - v_H(\mathbf{r}).$$

Here, ϵ'_1 corresponds to the constant (step) contribution to v_{xc} , while the remaining terms describe its spatially varying components.

Through the q-aufbau path, the step basis contribution to the exchange-correlation energy for each interval $m - 1 \rightarrow m$ is evaluated as:

$$E_{xc}^{\text{step}}[\rho_m] - E_{xc}^{\text{step}}[\rho_{m-1}] = \int d\mathbf{r} \int_0^1 v_{xc}^{\text{step}} \Delta\rho_m(\mathbf{r}) dq,$$

The overall contribution to the potential is the sum over all intervals:

$$E_{xc}^{\text{step}} = \sum_{m=1}^{N_e} (E_{xc}^{\text{step}, m-1 \rightarrow m})$$

The entire workflow, starting from the CI density (ρ_{WF}) to the computation of the exchange-correlation potential (v_{xc}), energy density (e_{xc}) and the step basis contribution to the exchange-correlation energy (E_{xc}^{step}), is summarized in Figure 1.

Computational Details

Electron densities were computed from Heat-Bath Configuration Interaction (HBCI) wavefunctions^{49–53} using a tight selection threshold (10^{-5} Ha for He-B, 5×10^{-5} Ha for C-Ne). These densities were converted to KS orbitals using the procedure outlined by Rask et al.³⁹ The exchange-correlation (XC) potentials were generated through the orbital-averaged inversion approach outlined in the previous section. For a system with N_e electrons, we computed the total exchange-correlation potential $v_{xc}^{\text{tot}} = v_{xc}^{\text{shape}} + v_{xc}^{\text{step}}$ over fractional electron counts, incrementally from 0 up to N_e . This was done over intervals $0 \rightarrow 1$, $1 \rightarrow 2$, and so forth, up to $N_e - 1 \rightarrow N_e$, using a 10th-order Gauss quadrature scheme. Details of the quadrature scheme are provided in the Supporting Information (SI) section S1.

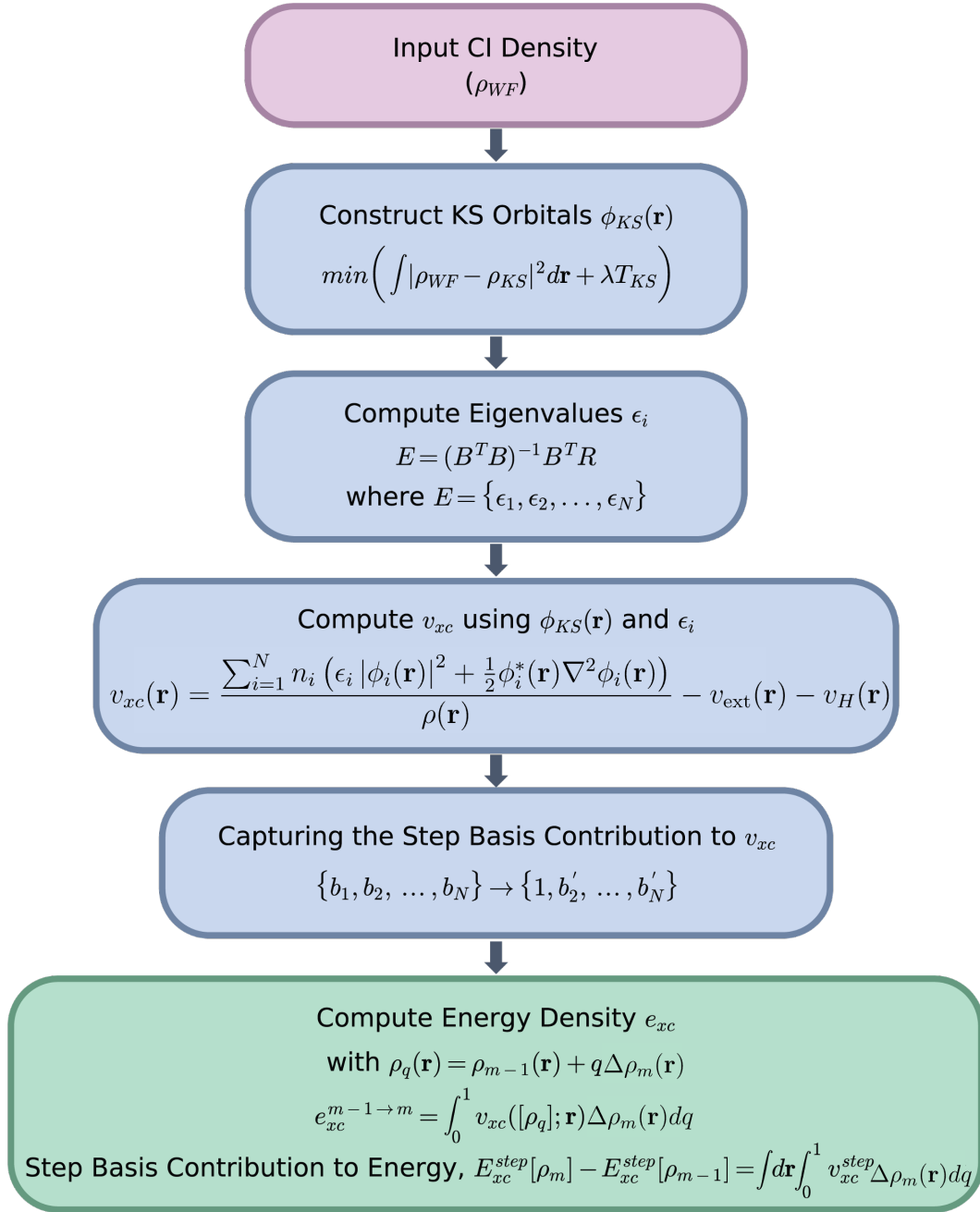


Figure 1: Workflow for computing the exchange correlation potential, step basis contribution, and energy density, starting from the CI electron density.

The Slater basis sets used in this work were constructed using an even-tempered approach following the method of Baerends and co-workers.⁵⁴ These basis sets included 14 1s, 9 2p, 7 3d and 2 4f functions (90 total functions). Integral evaluations in the Slater basis were performed using the SlaterGPU library.⁵⁵ Coulomb integrals were computed using the Resolution of the Identity (RI) approximation. The auxiliary basis, with a total of 245 functions, was constructed from the Slater exponents of the original basis through a procedure outlined in the SI section S2. The Kato cusp condition dictates the behavior of the electron density near the nucleus.⁵⁶ In this work, cusp corrections were performed using the modified self-consistent field (SCF) procedure described by Tribedi et al.^{35,57} More details about this can be found in the SI section S3.

The evaluation of STO integrals and the computation of the XC potential were performed on an atom-centered grid. This three-dimensional grid was constructed as a product of radial⁵⁸ and angular⁵⁹ points. For each atom, 600 radial points and 170 angular points were used in all calculations.

The entire workflow, from density generation to XC potential calculation, was implemented in C++ and leveraged OpenACC⁶⁰ for GPU acceleration. OpenACC directives were applied throughout the workflow, including within summation loops over grid points, to optimize performance on GPU resources. The `acc parallel` directive was used to efficiently parallelize calculations, enabling rapid evaluation of v_{xc} across the high-resolution spatial grid. Hartree and Slater potentials were computed through the RI basis, avoiding any 2e integrals.⁶¹

Convergence of the workflow was verified by minimizing the L_1 norm of the difference between the CI and KS densities $\Delta\rho_{L1}$, computed as $\int |\rho_{CI}(\mathbf{r}) - \rho_{KS}(\mathbf{r})| d\mathbf{r}$, and the magnitude of the residual $|R|$ from solving for KS eigenvalues.

For the KZG XC potential reported in this work, partial differential equation-constrained optimization (PDE-CO) was employed.²⁸⁻³⁰ The densities and potentials were discretized using an adaptively refined spectral finite-element (FE) basis. To address basis set errors

near the nuclei, a small correction $\Delta\rho$ defined as the difference between densities computed using the FE basis and the Slater basis was applied.²⁸

Expressions for PBE⁶² XC energy densities and their derivatives with respect to the electron density were obtained from the LibXC library.⁶³

Results and Discussion

This section begins with an evaluation of the quality of Kohn-Sham (KS) electron densities for atoms He-Ne by comparing them to the reference FCI densities. Then, the orbital-averaged exchange-correlation potentials are compared to the cusp-corrected KZG potentials^{28,29} and those from the PBE functional, and also evaluated through virial consistency tests. The asymptotic behavior of the computed v_{xc} is also examined. Later, the orbital-averaged v_{xc} and the step basis contributions for selected atoms are delineated. Finally, exchange-correlation energy densities (e_{xc}) from the q-aufbau path integral are reported.

Before delving into the comparison of computed densities and potentials, the characteristics and performance of the Slater basis sets used in this study are reported. This basis, comprising 14 1s, 9 2p, 7 3d, and 2 4f functions per atom, offers a detailed representation of the electron density due to its notable size and flexibility. The effectiveness of the Slater basis is evident from the small energy differences in the CI total energies computed with this basis compared to the cc-pCVTZ basis,⁶⁴ $\Delta E_{\text{per electron}}^{\text{Slater-cc-pCVTZ}}$, as reported in Table 2. Across the He-Ne series, the differences are on the order of 10^{-3} Ha per electron, with the largest deviation observed for oxygen (-1.495 mHa) and the smallest for beryllium (-0.771 mHa). As evident from the negative sign of $\Delta E_{\text{per electron}}^{\text{Slater-cc-pCVTZ}}$, CI energies with our Slater basis recover slightly more correlation than the cc-pCVTZ basis.

Table 2: Difference in CI total energies per electron, $\Delta E_{\text{per electron}}^{\text{Slater-cc-pCVTZ}}$, between calculations using the custom Slater basis set (with 14 1s, 9 2p, 7 3d, and 2 4f functions) and the cc-pCVTZ basis.⁶⁴ Units are mHa per electron.

Atom	$\Delta E_{\text{per electron}}^{\text{Slater-cc-pCVTZ}}$ (mHa)
He	-1.304
Li	-0.810
Be	-0.771
B	-1.131
C	-1.379
N	-1.443
O	-1.495
F	-1.260
Ne	-1.061

Evaluation of Computed KS Densities

The accuracy of the Kohn-Sham (KS) orbitals derived from Full Configuration Interaction (FCI) densities is assessed by comparing the KS electron densities with their FCI counterparts. Figure 2 illustrates the radial density differences, $\rho_{\text{FCI}} - \rho_{\text{KS}}$, for neutral atoms Be, B, N, and Ne. While the differences are most pronounced near the nucleus ($\mathbf{r} = 0$), where the electron density is highest, the relative error remains small. For example, the relative error for Ne is 6.12×10^{-5} at $\mathbf{r} = 0$, and the deviations quickly diminish at larger radial distances.

The L_1 norm of the density differences ($\Delta\rho_{L_1}$) provides a quantitative measure of agreement between FCI and KS densities. Table 3 summarizes the range of $\Delta\rho_{L_1}$ values per electron across all electron counts (both integer and fractional) from 0 to the total number of electrons in each atom. The $\Delta\rho_{L_1}$ values reported in Table 3 range from 10^{-4} to 10^{-3} per electron, highlighting the accuracy of the derived KS densities across a wide range of electron counts. For instance, $\Delta\rho_{L_1}$ ranges from 0.00023 to 0.00136 for Be and from 0.00018 to 0.00096 for Ne. These results confirm that the KS densities closely reproduce the FCI densities.

The KS densities remain consistent across λ values ranging from 10^{-5} to 10^{-4} , as shown for Be in Figure S1 of the Supporting Information. However, larger λ values lead to pro-

gressively larger $\Delta\rho_{L_1}$ values, reflecting the increasing influence of the kinetic energy term in the optimization. As with the prior study by Rask et al.,³⁹ relatively low values of λ are therefore preferred.

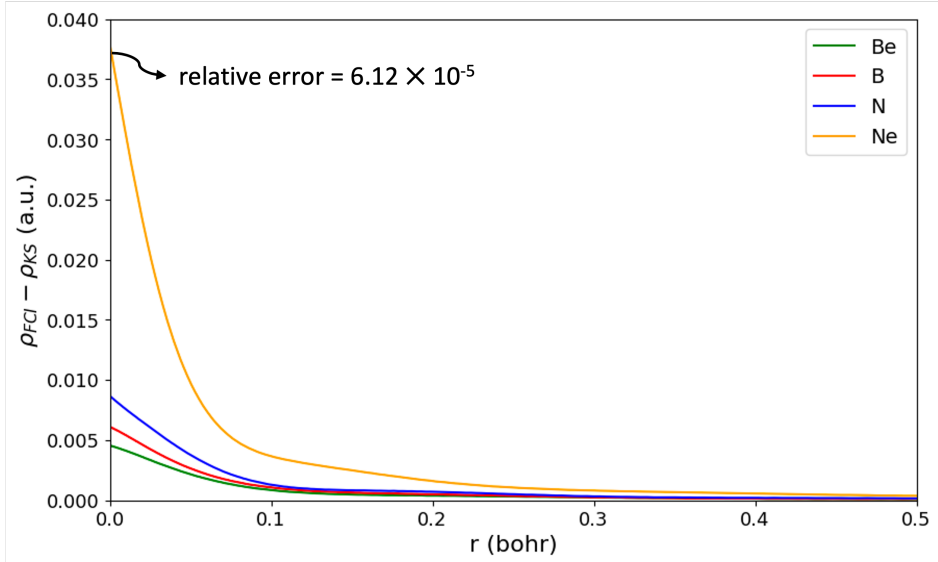


Figure 2: Difference in the FCI and KS densities for Be, B, N and Ne as a function of the radial distance.

Accuracy Tests for the Orbital-Averaged Potentials

The accuracy of the computed orbital-averaged exchange-correlation potentials (OA v_{xc}) was evaluated using several complementary tests, with details provided in the Supporting Information (SI). First, we investigated the influence of the mixing parameter λ , which controls the balance between density fitting and kinetic energy minimization in the formation of the KS orbitals from CI densities.³⁹ As discussed in the previous section, and in the SI (Section S4), higher λ values increase the weight of the kinetic energy term but degrade the density fit, leading to an increase in $\Delta\rho_{L_1}$ values. We observed that OA v_{xc} profiles were consistent across the domain for $\lambda = 0.00001$ to 0.0002 , except for regions close to the nucleus. As λ increases beyond 0.0001 , notable deviations emerge near the nucleus, reflecting the growing influence of the kinetic energy term in the optimization. These deviations manifest as sharp features, underscoring the difficulty of accurately modeling v_{xc} in this region, where

correlation-kinetic effects dominate.^{65–68} Based on these findings, we selected $\lambda = 0.00005$ for He through O and $\lambda = 0.0001$ for F and Ne, for all calculations in this work.

Next, we compared the computed OA v_{xc} with the cusp-corrected KZG potential for Be.^{28,30} As shown in Figure 3, the two potentials exhibit excellent agreement across the radial domain. Close to the nucleus, the KZG potential shows a slightly deeper potential and different slope. Beyond $r = 1$ bohr, where ρ decreases significantly, both potentials converge smoothly.

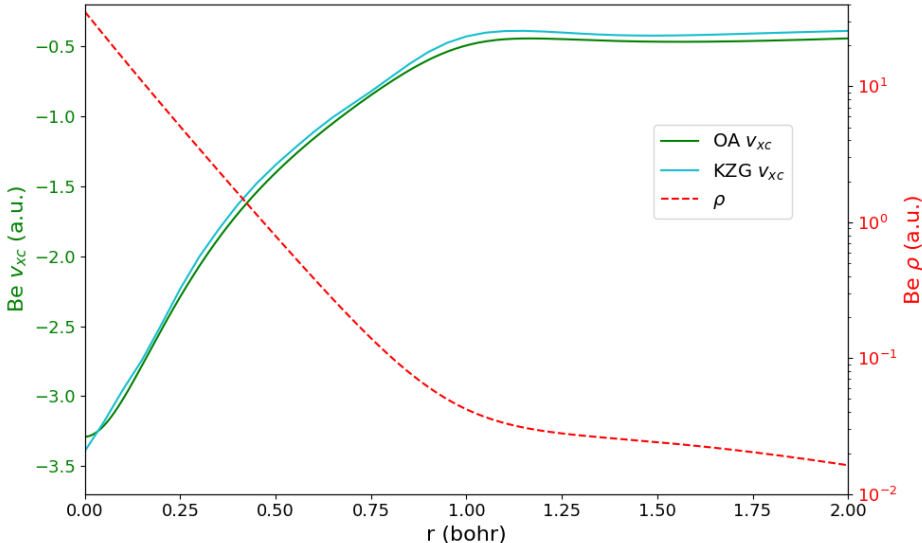


Figure 3: Comparison of the CI-derived orbital averaged exchange-correlation potential for Be with the KZG potential. The KS electron density is also shown in red.

The orbital-averaged potential was also benchmarked against the functional derivative of the PBE⁶² exchange-correlation functional for Ne, as detailed in Section S5 in the SI. Using KS orbitals derived from the PBE density, the OA v_{xc} was found to agree closely with the PBE functional derivative across most regions of space. Deviations were observed near the nucleus, where the functional derivative of PBE is unbounded.

Finally, the accuracy of the OA potentials were evaluated using the virial relation. Section S6 of the SI shows the virial of the XC potential, $t_{xc} = - \int \rho(\mathbf{r}) \mathbf{r} \cdot \nabla v_{xc}(\mathbf{r}) d\mathbf{r}$, and compares it to $E_{xc} + T_c$. The results, shown in Table S2 in the SI, demonstrate excellent agreement, with the largest deviation being 4.3 mHa. This consistency further confirms the accuracy of

the computed OA potentials.

Figure 4 shows the computed exchange-correlation potential for Be, B, N, and Ne as a function of $\log_{10} \mathbf{r}$. At large \mathbf{r} , all computed potentials exhibit the expected asymptotic behavior, decaying as $-1/\mathbf{r}$, in agreement with the known asymptotic of the potential.^{42,43} This decay of v_{xc} as $-1/\mathbf{r}$ ensures physically meaningful long-range behavior, for example it ensures an accurate HOMO energy, and consequently ionization energy (IE).⁴⁴ Hence, deviations from this behavior, often observed in LDA and generalized gradient approximation (GGA) functionals, lead to inaccuracies in predicted ionization energies.⁶⁹ Along with the correct asymptotic decay, the depth of v_{xc} near the nucleus increases with atomic number across the He–Ne series, consistent with the general features observed in SlaterRKS and KZG potentials.^{28,30,35} The use of a large Slater basis set is critical for achieving this accuracy. Unlike Gaussian basis sets, which often fail to accurately represent the electron density near the nucleus or at large distances, the Slater basis ensures the correct nuclear cusp and long-range decay, resulting in near-exact densities. This avoids the unphysical oscillations in the potential that arise during inversion when using Gaussian bases.^{19,25,70}

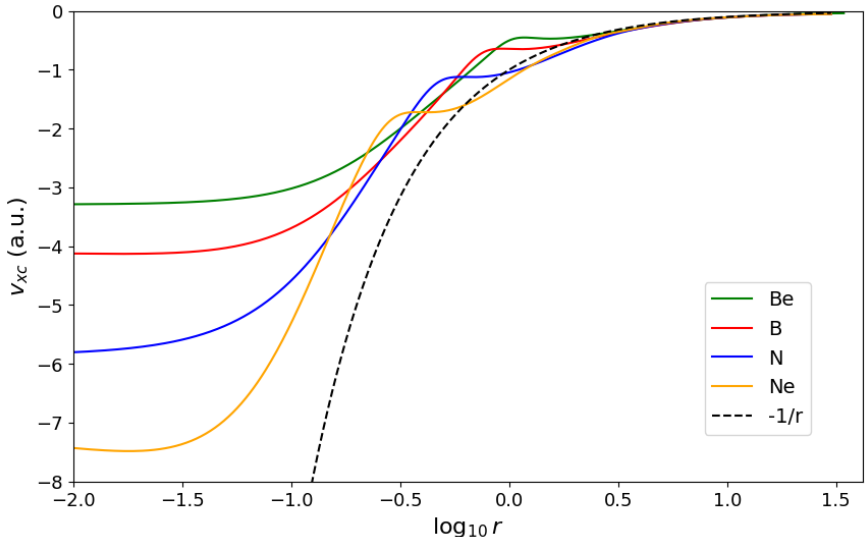


Figure 4: Exchange-correlation potential (v_{xc}) as a function of $\log_{10} \mathbf{r}$ (where \mathbf{r} is the radial distance in Bohr) for different atoms (Be, B, N, Ne). The black dashed line represents the asymptotic behavior $-1/\mathbf{r}$.

Table 3: Comparison of $\Delta\rho_{L_1}$, magnitude of residual $|R|$, and relative error in E_{xc} for various atoms, calculated across all electron counts (both integer and fractional) from 0 to the total number of electrons in each atom. $\Delta\rho_{L_1}$ is the L_1 norm of the difference between the CI and KS densities. $|R|$ represents the magnitude of the residual from solving for KS eigenvalues. The relative error in E_{xc} compares the E_{xc} obtained by integrating the energy density (e_{xc}) to the E_{xc} from CI calculations. Across the He-Ne series, the error in the predicted ionization energy, $|I^{CI}| - |\epsilon_{HOMO}^{KS}|$, was found to be $< 10^{-6}$.

Atom	$\Delta\rho_{L_1}$ range (per electron)	Maxium $ R $ (per occupied orbital)	$ \Delta E_{xc}/E_{xc}^{CI} $
He	0.000293 – 0.000886	0.000000	0.000187
Li	0.000296 – 0.001949	0.000085	0.000054
Be	0.000225 – 0.001361	0.000066	0.000180
B	0.000193 – 0.001065	0.000494	0.000619
C	0.000163 – 0.000857	0.001156	0.000250
N	0.000145 – 0.000748	0.001516	0.000059
O	0.000123 – 0.000645	0.001608	0.000548
F	0.000210 – 0.001069	0.001138	0.000077
Ne	0.000182 – 0.000958	0.001972	0.000999

Orbital-Averaged Potentials Across Electron Counts

Exchange-correlation potentials were computed for He through Ne for all electron counts, including neutral atoms and positively charged species. Potentials were computed for both integer and fractional charges. The fractional electron counts within each interval $m-1 \rightarrow m$ (where $m = 1, 2, \dots, N_e$ for an atom with N_e electrons) were sampled using the 10-point quadrature shown in the SI section S1.

Table 3 summarizes the quantitative accuracy of the computed KS quantities across all electron counts. The L_1 norms of the density differences ($\Delta\rho_{L_1}$) range between 10^{-4} and 10^{-3} per electron for most systems, reflecting the close agreement between the KS densities and the reference FCI densities. Li exhibits slightly larger $\Delta\rho_{L_1}$ values (0.000296 to 0.001949), which can be attributed to the diffuse nature of its 2s electron. Across the He-Ne series, $|R|$ remains small, with the maximum value being only 0.001972, partly indicating the accuracy of the computed KS eigenvalues.

Figure 5 shows three-dimensional plots of OA v_{xc} as a function of the radial distance \mathbf{r}

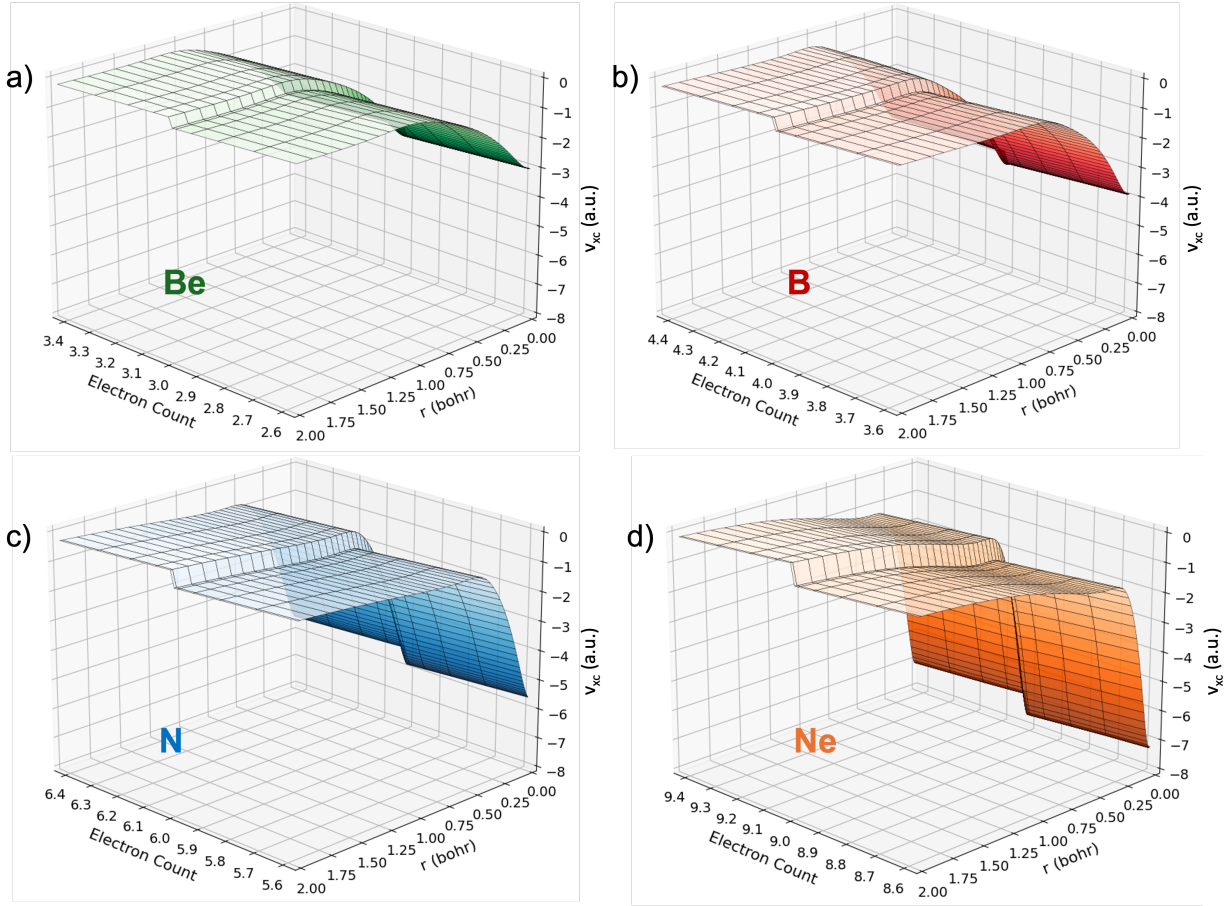


Figure 5: Three-dimensional plots of the exchange-correlation potential (v_{xc}) for a) Be, b) B, c) N, and d) Ne as functions of the radial distance (\mathbf{r}) and electron count. The electron count is defined as $N_e - 1 + a$, where a spans fractional values between -0.5 and 0.5 for an atom with N_e electrons.

and electron count $N_e - 1 + a$, where a spans fractional values between -0.5 and 0.5 for an atom with N_e electrons. A key feature of these plots is the step in v_{xc} that occurs as the electron count crosses an integer. This step is a hallmark of the exact exchange-correlation potential,^{47,48} arising from the derivative discontinuity of the total energy. As evident from Figure 5, the height of the step in the potential on crossing the $(N_e - 1)$ th electron, measuring the magnitude of the derivative discontinuity, increases significantly when moving from Be to Ne. Commonly used approximations, such as the Local Density Approximation (LDA) and Generalized Gradient Approximation (GGA), smooth over this transition, leading to significant inaccuracies. These approximations often underestimate energy gaps and fail to describe dissociation limits.^{71–73}

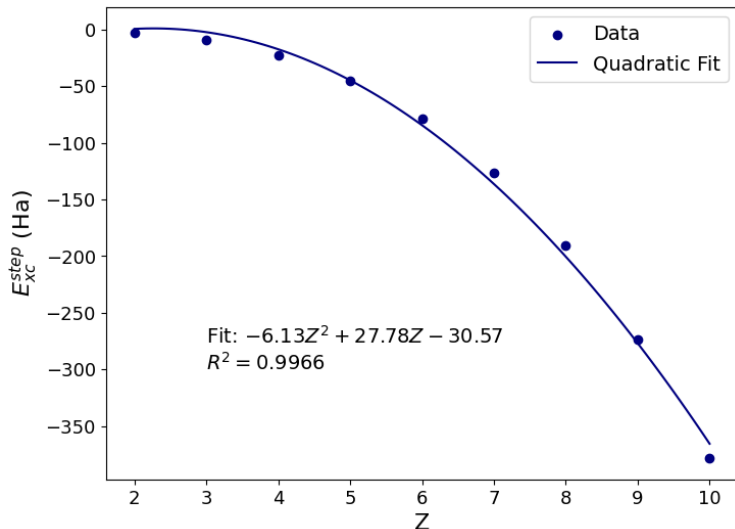


Figure 6: Variation of the step basis contribution to the exchange-correlation energy with atomic number Z . The quadratic fitting was done while imposing a penalty on positive slopes.

Figure 6 illustrates the variation of the step basis contribution to the exchange-correlation energy (E_{xc}^{step}) as a function of atomic number (Z). The data is well described by a quadratic fit,

$$E_{xc}^{\text{step}} = -6.13Z^2 + 27.78Z - 30.57,$$

with an $R^2 = 0.9966$.

This quadratic scaling of E_{xc}^{step} with Z complements the findings of Hait and Head-

Gordon,⁷⁴ who investigated delocalization errors in density functional approximations (DFAs). Hait and Head-Gordon demonstrated that the delocalization energy error in DFAs exhibits a quadratic dependence on fractional electron count, and attributed it majorly to residual self-repulsion seen in approximate functionals.⁷⁴ The step basis contribution to the exchange-correlation energy in this study therefore complements their analysis, specifically by providing a benchmark for the step contribution that should be present in an accurate DFA. Our relationship between E_{xc}^{step} and atomic number Z can be linked to its dependence on ϵ'_1 , which reflects the ionization energies of each atom. This energy scales approximately quadratically (this is an exact dependence in hydrogen-like atoms), where the balance of electrostatic attraction and kinetic energy results in energy levels proportional to $-Z^2$ (c.f. Figure S3 in the SI). This parallelity suggests that the energetics of the total step basis contribution are closely related to the physical principles that dominate total ionization energy scaling.

Exchange-Correlation Energy Densities from Orbital-Averaged Potentials

Exchange-correlation energy densities, e_{xc} , were computed using the orbital-averaged v_{xc} along the q-aufbau path. Figure 7 illustrates the radial variation of $\log_{10}|e_{xc}|$ alongside $\log_{10}\rho$ for Be, B, N, and Ne. Close to the nucleus, e_{xc} closely reflects the behavior of $\rho(\mathbf{r})$, with steep gradients and sharp peaks. This behavior arises not only from the weighting by the density in the line integral formulation but also from the large magnitude of v_{xc} in this region. These features are particularly evident in heavier atoms like Ne, where the larger nuclear charge results in a more localized and pronounced e_{xc} . From intermediate to large radial distances, e_{xc} essentially follows the same behavior as ρ , dropping more rapidly for Ne than for Be. This behavior mirrors the decay of the electron density itself, explaining the observed crossing of e_{xc} lines across atoms in this region.

The total E_{xc} values, obtained by integrating these energy densities, show excellent agreement with reference CI values across the He–Ne series. As summarized in Table 3, the relative

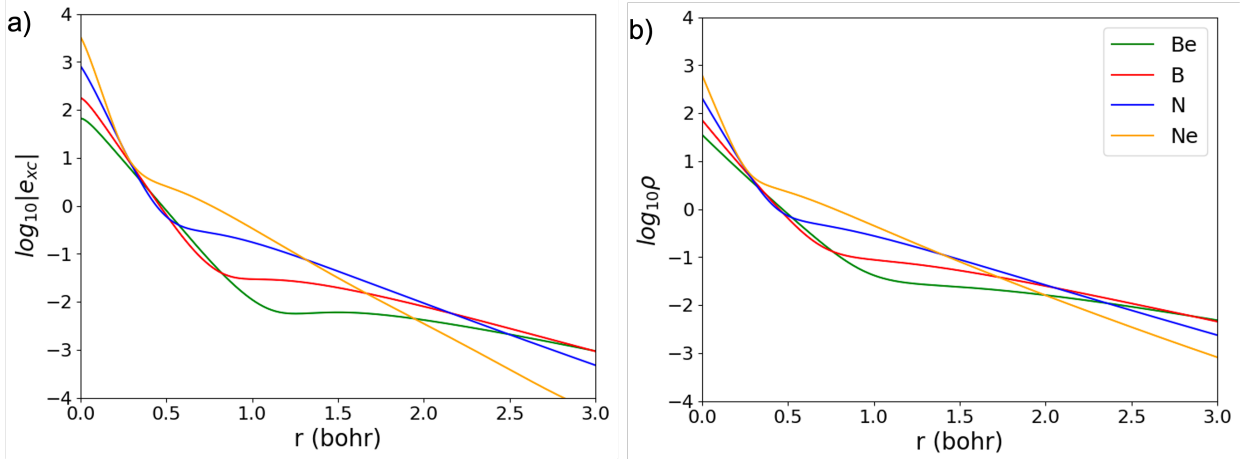


Figure 7: Plots depicting the variation of a) $\log_{10} |e_{xc}|$ and b) $\log_{10} \rho$ for Be, B, N, Ne with the radial distance (\mathbf{r}).

error $|\Delta E_{xc}/E_{xc}^{CI}|$ remains consistently below 0.1%, demonstrating the high accuracy of the computed exchange-correlation energy densities for the He to Ne series.

Figure 8 illustrates the variation of $\log_{10} |e_{xc}|$ with respect to $\log_{10} \rho$ and $\log_{10} |\nabla \rho|$ for Be, B, N, and Ne. Panel (a) shows results derived from the PBE functional,⁶² while panel (b) corresponds to e_{xc} computed using the orbital-averaged v_{xc} obtained from FCI densities. Across both cases, e_{xc} values are pronounced in regions of high density and density gradients, with broad similarities in magnitude between PBE and FCI-derived energy densities.

More detailed comparisons between PBE and the precise e_{xc} distributions of this work are not straightforward to make. PBE is inexact, with energy densities that do not integrate to the FCI values, and PBE is in a different gauge than the q-aufbau path. Regardless, we find it remarkable that the q-aufbau path has e_{xc} features that qualitatively resemble PBE, despite the known, significant differences in v_{xc} .^{75,76}

Conclusions

This work introduces an accurate framework for computing the exchange-correlation potential (v_{xc}) and energy densities (e_{xc}) from CI-derived KS orbitals. By using a large Slater basis set, the workflow avoids the oscillatory artifacts and inaccuracies that often arise in

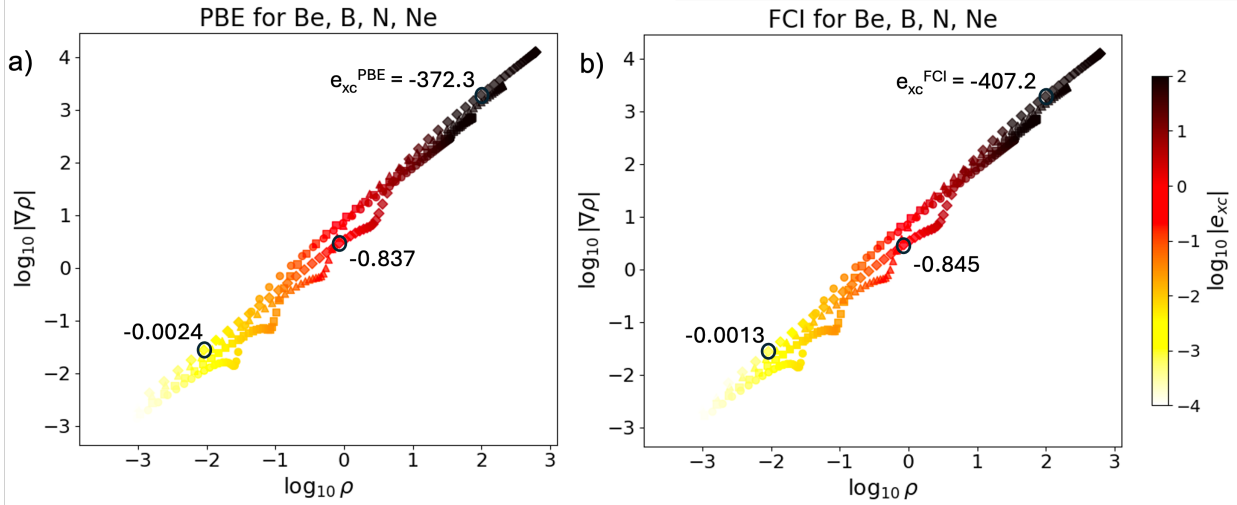


Figure 8: Scatter plots of $\log_{10} |\nabla\rho|$ versus $\log_{10} \rho$ for Be, B, N, Ne. The colormaps represent $\log_{10} |e_{xc}|$ values from a) PBE and b) FCI. Select e_{xc} values for Ne have been labeled on both plots.

KS inversions using other finite basis sets. By applying this framework to the He-Ne series, we have demonstrated its ability to capture key features of the exact potential, including the correct asymptotic $-1/r$ decay, behavior near the nucleus, and the discontinuous step as the electron count crosses an integer.

The ability to extract this step in the potential, and the step basis contribution to the exchange-correlation energy (E_{xc}^{step}) directly from first principles provides a systematic benchmark for improving density functional approximations.^{48,77-79} By incorporating step-like features and their quadratic scaling into future designs, XC functionals could address the deficiencies in capturing derivative discontinuities and provide more accurate predictions for properties such as ionization potentials, energy gaps, and dissociation limits.^{80,81}

In addition to the step, this study provides accurate exchange-correlation energy densities, from OA v_{xc} using the q-aufbau path, for the He-Ne series. By leveraging these, new functionals can be designed whose energy densities integrate to the correct E_{xc} , and reproduce the exact v_{xc} , thereby encoding non-local features that are critical for accurate chemical predictions. The ability to incorporate exact exchange-correlation behavior into functional design promises to bridge the gap between wavefunction-level accuracy and the

computational efficiency of density functional theory.

Acknowledgement

This project has been supported by the Department of Energy through the grant DE-SC0022241.

Supporting Information Available

More details about the Gauss quadrature, auxiliary basis set, cusp correction, impact of parameter λ on the computed XC potentials, comparison of the PBE orbital-averaged v_{xc} with the functional derivative of PBE, the virial of the potential, and quadratic scaling of total ionization energy can be found in the supporting information.

References

- (1) Becke, A. D. Perspective: Fifty years of density-functional theory in chemical physics. *J. Chem. Phys.* **2014**, *140*, 18A301.
- (2) Cramer, C. J.; Truhlar, D. G. Density functional theory for transition metals and transition metal chemistry. *Phys. Chem. Chem. Phys.* **2009**, *11*, 10757–10816.
- (3) Khanna, V.; Singh, R.; Claes, P.; Nguyen, M. T.; Fielicke, A.; Janssens, E.; Lievens, P.; McGrady, J. E. Evolution of Vibrational Spectra in the Manganese–Silicon Clusters Mn_2Si_n , $n = 10, 12$, and 13 , and Cationic $[\text{Mn}_2\text{Si}_{13}]^+$. *J. Phys. Chem. A* **2022**, *126*, 1617–1626.
- (4) Perdew, J. P.; Ruzsinszky, A.; Csonka, G. I.; Vydrov, O. A.; Scuseria, G. E.; Constantin, L. A.; Zhou, X.; Burke, K. Restoring the Density-Gradient Expansion for Exchange in Solids and Surfaces. *Phys. Rev. Lett.* **2008**, *100*, 136406.

- (5) Hasnip, P. J.; Refson, K.; Probert, M. I. J.; Yates, J. R.; Clark, S. J.; Pickard, C. J. Density functional theory in the solid state. *Philos. Trans. R. Soc. A* **2014**, *372*, 20130270.
- (6) Khanna, V.; Kanungo, B.; Gavini, V.; Tewari, A.; Zimmerman, P. M. Examining the Impact of Local Constraint Violations on Energy Computations in DFT. *J. Comput. Chem.* **2025**, *46*, e70005.
- (7) Teale, A. M. et al. DFT exchange: sharing perspectives on the workhorse of quantum chemistry and materials science. *Phys. Chem. Chem. Phys.* **2022**, *24*, 28700–28781.
- (8) Kohn, W.; Sham, L. J. Self-Consistent Equations Including Exchange and Correlation Effects. *Phys. Rev.* **1965**, *140*, A1133–A1138.
- (9) Mardirossian, N.; Head-Gordon, M. Thirty years of density functional theory in computational chemistry: an overview and extensive assessment of 200 density functionals. *Mol. Phys.* **2017**, *115*, 2315–2372.
- (10) Yang, W.; Wu, Q. Direct Method for Optimized Effective Potentials in Density-Functional Theory. *Phys. Rev. Lett.* **2002**, *89*, 143002.
- (11) Gidopoulos, N. I.; Lathiotakis, N. N. Nonanalyticity of the optimized effective potential with finite basis sets. *Phys. Rev. A* **2012**, *85*, 052508.
- (12) Gould, T. Toward routine Kohn–Sham inversion using the “Lieb-response” approach. *J. Chem. Phys.* **2023**, *158*, 064102.
- (13) Gould, T.; Toulouse, J. Kohn-Sham potentials in exact density-functional theory at noninteger electron numbers. *Phys. Rev. A* **2014**, *90*, 050502.
- (14) Trushin, E.; Erhard, J.; Görling, A. Violations of the v -representability condition underlying Kohn-Sham density-functional theory. *Phys. Rev. A* **2024**, *110*, L020802.
- (15) Erhard, J.; Trushin, E.; Görling, A. Kohn–Sham inversion for open-shell systems. *J. Chem. Phys.* **2025**, *162*, 034116.

- (16) Trushin, E.; Fauser, S.; Mölkner, A.; Erhard, J.; Görling, A. Accurate Correlation Potentials from the Self-Consistent Random Phase Approximation. *Phys. Rev. Lett.* **2025**, *134*, 016402.
- (17) Bulat, F. A.; Heaton-Burgess, T.; Cohen, A. J.; Yang, W. Optimized effective potentials from electron densities in finite basis sets. *J. Chem. Phys.* **2007**, *127*, 174101.
- (18) Heaton-Burgess, T.; Yang, W. Optimized effective potentials from arbitrary basis sets. *J. Chem. Phys.* **2008**, *129*, 194102.
- (19) Shi, Y.; Wasserman, A. Inverse Kohn–Sham Density Functional Theory: Progress and Challenges. *J. Phys. Chem. Lett.* **2021**, *12*, 5308–5318.
- (20) Ryabinkin, I. G.; Ospadov, E.; Staroverov, V. N. Exact exchange-correlation potentials of singlet two-electron systems. *J. Chem. Phys.* **2017**, *147*, 164117.
- (21) Aryasetiawan, F.; Stott, M. Effective potentials in density-functional theory. *Phys. Rev. B* **1988**, *38*, 2974–2981.
- (22) Görling, A. Kohn-Sham potentials and wave functions from electron densities. *Phys. Rev. A* **1992**, *46*, 3753–3757.
- (23) Zhao, Q.; Parr, R. G. Quantities $T_s[n]$ and $T_c[n]$ in density-functional theory. *Phys. Rev. A* **1992**, *46*, 2337–2339.
- (24) Zhao, Q.; Parr, R. G. Constrained-search method to determine electronic wave functions from electronic densities. *J. Chem. Phys.* **1993**, *98*, 543–548.
- (25) Jensen, D. S.; Wasserman, A. Numerical methods for the inverse problem of density functional theory. *Int. J. Quantum Chem.* **2017**, *118*, e25425.
- (26) Wang, Y.; Parr, R. G. Construction of exact Kohn-Sham orbitals from a given electron density. *Phys. Rev. A* **1993**, *47*, R1591–R1593.

- (27) Peirs, K.; Van Neck, D.; Waroquier, M. Algorithm to derive exact exchange-correlation potentials from correlated densities in atoms. *Phys. Rev. A* **2003**, *67*, 012505.
- (28) Kanungo, B.; Zimmerman, P.; Gavini, V. Exact exchange-correlation potentials from ground-state electron densities. *Nat. Commun.* **2019**, *10*, 4497.
- (29) Kanungo, B.; Tribedi, S.; Zimmerman, P. M.; Gavini, V. Accelerating inverse Kohn-Sham calculations using reduced density matrices. 2024; <https://arxiv.org/abs/2408.02342>.
- (30) Kanungo, B.; Hatch, J.; Zimmerman, P. M.; Gavini, V. Exact and Model Exchange-Correlation Potentials for Open-Shell Systems. *J. Phys. Chem. Lett.* **2023**, *14*, 10039–10045.
- (31) Stückrath, J. B.; Bischoff, F. A. Reduction of Hartree–Fock Wavefunctions to Kohn–Sham Effective Potentials Using Multiresolution Analysis. *J. Chem. Theory Comput.* **2021**, *17*, 1408–1420.
- (32) Ryabinkin, I. G.; Kohut, S. V.; Staroverov, V. N. Reduction of Electronic Wave Functions to Kohn-Sham Effective Potentials. *Phys. Rev. Lett.* **2015**, *115*, 083001.
- (33) Cuevas-Saavedra, R.; Ayers, P. W.; Staroverov, V. N. Kohn–Sham exchange-correlation potentials from second-order reduced density matrices. *J. Chem. Phys.* **2015**, *143*, 244116.
- (34) Ospadov, E.; Ryabinkin, I. G.; Staroverov, V. N. Improved method for generating exchange-correlation potentials from electronic wave functions. *J. Chem. Phys.* **2017**, *146*, 084103.
- (35) Tribedi, S.; Dang, D.-K.; Kanungo, B.; Gavini, V.; Zimmerman, P. M. Exchange correlation potentials from full configuration interaction in a Slater orbital basis. *J. Chem. Phys.* **2023**, *159*, 054106.

- (36) van Leeuwen, R.; Baerends, E. J. Exchange-correlation potential with correct asymptotic behavior. *Phys. Rev. A* **1994**, *49*, 2421–2431.
- (37) Gritsenko, O. V.; van Leeuwen, R.; Baerends, E. J. Molecular Kohn-Sham exchange-correlation potential from the correlated ab initio electron density. *Phys. Rev. A* **1995**, *52*, 1870–1874.
- (38) Kananenka, A. A.; Kohut, S. V.; Gaiduk, A. P.; Ryabinkin, I. G.; Staroverov, V. N. Efficient construction of exchange and correlation potentials by inverting the Kohn–Sham equations. *J. Chem. Phys.* **2013**, *139*, 074112.
- (39) Rask, A. E.; Li, L.; Zimmerman, P. M. Kohn–Sham Density in a Slater Orbital Basis Set. *J. Phys. Chem. A* **2024**, *128*, 3194–3204.
- (40) Levy, M.; Perdew, J. P. Hellmann-Feynman, virial, and scaling requisites for the exact universal density functionals. Shape of the correlation potential and diamagnetic susceptibility for atoms. *Phys. Rev. A* **1985**, *32*, 2010–2021.
- (41) Gaiduk, A. P.; Chulkov, S. K.; Staroverov, V. N. Reconstruction of Density Functionals from Kohn Sham Potentials by Integration along Density Scaling Paths. *J. Chem. Theory Comput.* **2009**, *5*, 699–707.
- (42) Schmidt, T.; Kraisler, E.; Kronik, L.; Kümmel, S. One-electron self-interaction and the asymptotics of the Kohn–Sham potential: an impaired relation. *Phys. Chem. Chem. Phys.* **2014**, *16*, 14357–14367.
- (43) Wu, Q.; Ayers, P. W.; Yang, W. Density-functional theory calculations with correct long-range potentials. *J. Chem. Phys.* **2003**, *119*, 2978–2990.
- (44) Kraisler, E. Asymptotic Behavior of the Exchange-Correlation Energy Density and the Kohn-Sham Potential in Density Functional Theory: Exact Results and Strategy for Approximations. *Isr. J. Chem.* **2020**, *60*, 805–822.

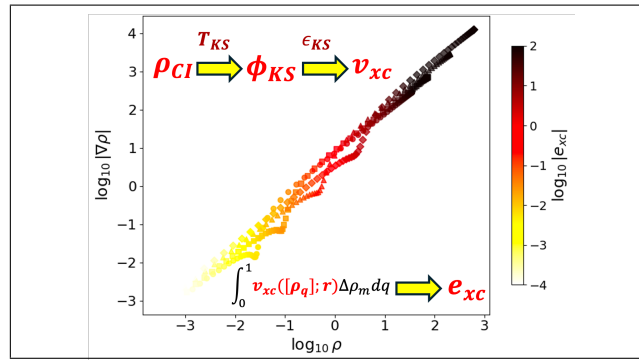
- (45) van Leeuwen, R.; Baerends, E. J. Energy expressions in density-functional theory using line integrals. *Phys. Rev. A* **1995**, *51*, 170–178.
- (46) Elkind, P. D.; Staroverov, V. N. Energy expressions for Kohn–Sham potentials and their relation to the Slater–Janak theorem. *J. Chem. Phys.* **2012**, *136*, 124115.
- (47) Perdew, J. P.; Parr, R. G.; Levy, M.; Balduz, J. L. Density-Functional Theory for Fractional Particle Number: Derivative Discontinuities of the Energy. *Phys. Rev. Lett.* **1982**, *49*, 1691–1694.
- (48) Yang, W.; Cohen, A. J.; Mori-Sánchez, P. Derivative discontinuity, bandgap and lowest unoccupied molecular orbital in density functional theory. *J. Chem. Phys.* **2012**, *136*, 204111.
- (49) Holmes, A. A.; Tubman, N. M.; Umrigar, C. J. Heat-bath configuration interaction: An efficient selected configuration interaction algorithm inspired by heat-bath sampling. *J. Chem. Theory Comput.* **2016**, *12*, 3674–3680.
- (50) Sharma, S.; Holmes, A. A.; Jeanmairet, G.; Alavi, A.; Umrigar, C. J. Semistochastic heat-bath configuration interaction method: Selected configuration interaction with semistochastic perturbation theory. *J. Chem. Theory Comput.* **2017**, *13*, 1595–1604.
- (51) Li, J.; Otten, M.; Holmes, A. A.; Sharma, S.; Umrigar, C. J. Fast semistochastic heat-bath configuration interaction. *J. Chem. Phys.* **2018**, *149*, 214110.
- (52) Dang, D.-K.; Kammeraad, J. A.; Zimmerman, P. M. Advances in parallel heat bath configuration interaction. *J. Phys. Chem. A* **2023**, *127*, 400–411.
- (53) Chien, A. D.; Holmes, A. A.; Otten, M.; Umrigar, C. J.; Sharma, S.; Zimmerman, P. M. Excited states of methylene, polyenes, and ozone from heat-bath configuration interaction. *J. Phys. Chem. A* **2018**, *122*, 2714–2722.

- (54) Lenthe, E. V.; Baerends, E. J. Optimized Slater-type basis sets for the elements 1–118. *J. Comput. Chem.* **2003**, *24*, 1142–1156.
- (55) Dang, D.-K.; Wilson, L. W.; Zimmerman, P. M. The numerical evaluation of Slater integrals on graphics processing units. *J. Comput. Chem.* **2022**, *43*, 1680–1689.
- (56) Kato, T. On the eigenfunctions of many-particle systems in quantum mechanics. *Comm. Pure Appl. Math.* **1957**, *10*, 151–177.
- (57) Handy, N. C. The molecular physics lecture 2004: (i) Density functional theory, (ii) Quantum Monte Carlo. *Mol. Phys.* **2004**, *102*, 2399–2409.
- (58) Mura, M. E.; Knowles, P. J. Improved radial grids for quadrature in molecular density-functional calculations. *J. Chem. Phys.* **1996**, *104*, 9848–9858.
- (59) Lebedev, V. Quadratures on a sphere. *USSR Comput. Math. Math. Phys.* **1976**, *16*, 10–24.
- (60) The OpenACC Application Programming Interface, Version 3.3. OpenACC Organization, 2022.
- (61) Cohen, A. J.; Handy, N. C. Density functional generalized gradient calculations using Slater basis sets. *J. Chem. Phys.* **2002**, *117*, 1470–1478.
- (62) Perdew, J. P.; Burke, K.; Ernzerhof, M. Generalized Gradient Approximation Made Simple. *Phys. Rev. Lett.* **1996**, *77*, 3865–3868.
- (63) Lehtola, S.; Steigemann, C.; Oliveira, M. J.; Marques, M. A. Recent developments in libxc — A comprehensive library of functionals for density functional theory. *SoftwareX* **2018**, *7*, 1–5.
- (64) Woon, D. E.; Dunning, J., Thom H. Gaussian basis sets for use in correlated molecular calculations. V. Core-valence basis sets for boron through neon. *J. Chem. Phys.* **1995**, *103*, 4572–4585.

- (65) Qian, Z.; Sahni, V. Asymptotic near-nucleus structure of the electron-interaction potential in local effective potential theories. *Phys. Rev. A* **2007**, *75*, 032517.
- (66) Qian, Z. Exchange and correlation near the nucleus in density functional theory. *Phys. Rev. B* **2007**, *75*, 193104.
- (67) Moore, C. C.; Staroverov, V. N. Jump discontinuities of finite-basis-set exchange–correlation potentials at atomic nuclei. *J. Chem. Phys.* **2024**, *161*, 124106.
- (68) Moore, C. C.; Staroverov, V. N. Are Exact Exchange–Correlation Potentials Continuous at Atomic Nuclei in Molecules? *J. Chem. Theory Comput.* **2024**, *20*, 8934–8939.
- (69) Staroverov, V. N.; Scuseria, G. E.; Tao, J.; Perdew, J. P. Tests of a ladder of density functionals for bulk solids and surfaces. *Phys. Rev. B* **2004**, *69*, 075102.
- (70) Gaiduk, A. P.; Ryabinkin, I. G.; Staroverov, V. N. Removal of Basis-Set Artifacts in Kohn–Sham Potentials Recovered from Electron Densities. *J. Chem. Theory Comput.* **2013**, *9*, 3959–3964.
- (71) Cohen, A. J.; Mori-Sánchez, P.; Yang, W. Fractional spins and static correlation error in density functional theory. *J. Chem. Phys.* **2008**, *129*, 121104.
- (72) Baerends, E.; Gritsenko, O.; van Meer, R. The Kohn–Sham gap, the fundamental gap, and the optical gap: The physical meaning of occupied and virtual Kohn–Sham orbital energies. *Phys. Chem. Chem. Phys.* **2013**, *15*, 16408–16425.
- (73) Hellgren, M.; Gross, E. K. U. Discontinuities of the exchange–correlation kernel and charge–transfer excitations in time–dependent density–functional theory. *Phys. Rev. A* **2012**, *85*, 022514.
- (74) Hait, D.; Head-Gordon, M. Delocalization Errors in Density Functional Theory Are Essentially Quadratic in Fractional Occupation Number. *J. Phys. Chem. Lett.* **2018**, *9*, 6280–6288.

- (75) Gaiduk, A. P.; Staroverov, V. N. Construction of integrable model Kohn-Sham potentials by analysis of the structure of functional derivatives. *Phys. Rev. A* **2011**, *83*, 012509.
- (76) Kanungo, B.; Zimmerman, P. M.; Gavini, V. A Comparison of Exact and Model Exchange–Correlation Potentials for Molecules. *J. Phys. Chem. Lett.* **2021**, *12*, 12012–12019.
- (77) Mori-Sánchez, P.; Cohen, A. J.; Yang, W. Localization and Delocalization Errors in Density Functional Theory and Implications for Band-Gap Prediction. *Phys. Rev. Lett.* **2008**, *100*, 146401.
- (78) Chan, G. K.-L. A fresh look at ensembles: Derivative discontinuities in density functional theory. *J. Chem. Phys.* **1999**, *110*, 4710–4723.
- (79) Baerends, E. J. Chemical potential, derivative discontinuity, fractional electrons, jump of the Kohn–Sham potential, atoms as thermodynamic open systems, and other (mis)conceptions of the density functional theory of electrons in molecules. *Phys. Chem. Chem. Phys.* **2022**, *24*, 12745–12766.
- (80) Cohen, A. J.; Mori-Sánchez, P.; Yang, W. Challenges for Density Functional Theory. *Chem. Rev.* **2012**, *112*, 289–320.
- (81) Hodgson, M. J. P.; Kraisler, E.; Schild, A.; Gross, E. K. U. How Interatomic Steps in the Exact Kohn–Sham Potential Relate to Derivative Discontinuities of the Energy. *J. Phys. Chem. Lett.* **2017**, *8*, 5974–5980.

TOC Graphic



Supporting Information: Exchange-Correlation Potentials and Energy Densities through Orbital Averaging and Aufbau Integration

Vaibhav Khanna,[†] Bikash Kanungo,[‡] Jeffrey Hatch,[†] Joshua Kammeraad,[†] and
Paul M. Zimmerman^{*,†}

[†]*Department of Chemistry, University of Michigan, Ann Arbor, Michigan 48109, United States*

[‡]*Department of Mechanical Engineering, University of Michigan, Ann Arbor, Michigan 48109, United States*

E-mail: paulzim@umich.edu

Table of Contents

- Gauss Quadrature Points and Weights S3
- Auxiliary Basis Construction S3
- Enforcing the Cusp Condition S4
- XC Potentials Close to the Nucleus: Impact of λ S4
- Comparison of the PBE orbital-averaged (OA) v_{xc} with the PBE functional derivative for Ne S6
- Virial of the XC potential S6
- Quadratic Scaling of Total Ionization Energy S7

S1. Gauss Quadrature Points and Weights

For a system with N_e electrons, we computed the total exchange-correlation potential $v_{xc}^{\text{tot}} = v_{xc}^{\text{shape}} + v_{xc}^{\text{step}}$ over fractional electron counts, incrementally from 0 up to N_e . This was done over intervals $0 \rightarrow 1$, $1 \rightarrow 2$, and so forth, up to $N_e - 1 \rightarrow N_e$, using quadrature. The 10th-order Gauss quadrature points and weights used in this work are listed in Table S1.

Table S1: Gauss quadrature points (e_i) and weights (w_i).

e_i (Quadrature Points)	w_i (Weights)
0.0130467357	0.0333356722
0.0674683167	0.0747256746
0.1602952159	0.1095431813
0.2833023029	0.1346333597
0.4255628305	0.1477621124
0.5744371695	0.1477621124
0.7166976971	0.1346333597
0.8397047841	0.1095431813
0.9325316833	0.0747256746
0.9869532643	0.0333356722

S2. Auxiliary Basis Construction

The auxiliary basis, with a total of 245 functions, was constructed from the Slater exponents of the original basis. Auxiliary functions were generated pairwise, combining the exponents of functions within the same or different angular momentum types. For example, S -type auxiliary functions were constructed by combining S -type exponents from the original basis, while P -type auxiliary functions were derived from combinations of S - and P -type exponents. Similarly, D -type auxiliary functions were generated from P -type combinations, with analogous processes applied for higher angular momentum types. For each angular momentum channel, the minimum and maximum Slater exponents (ζ_{min} and ζ_{max}) were selected to define the range for the auxiliary basis. Within this range, additional exponents were introduced using an even-tempered scheme. The total number of exponents was determined based on the spread between ζ_{min} and ζ_{max} , with more functions being generated for wider

zeta ranges. The resulting basis had 12 S functions, 12 P, 8 D, 6 F, and 3 G and 8 H functions.

S3. Enforcing the Cusp Condition

The Kato cusp condition dictates the behavior of the electron density near the nucleus.¹ Following the procedure described by Tribedi et al.,^{2,3} we modified the self-consistent field (SCF) equations so that the orbitals satisfy Kato’s nuclear cusp condition:

$$\left. \frac{\partial \phi_i}{\partial \mathbf{r}} \right|_{\mathbf{r}=\mathbf{R}_A} = -Z_A \phi_i(\mathbf{R}_A),$$

where \mathbf{R}_A is the position of the nucleus A with atomic number Z_A .^{2,3} The SCF procedure was modified as:

$$[(I - A)(F - \varepsilon S)(I - A)]c = 0,$$

where

$$A = \sum_{BC} \hat{p}_B (\hat{p}_B^T \hat{p}_C)^{-1} \hat{p}_C^T.$$

See Refs [2] and [3] for further details of how the projector is constructed based on the Kato condition.

S4. XC Potentials Close to the Nucleus: Impact of λ

Figure S1 illustrates the effect of the mixing parameter λ on the computed exchange-correlation potentials v_{xc} for beryllium (Be). In the Rask procedure,⁴ λ controls the contribution of the kinetic energy term in the objective function used to obtain KS orbitals from FCI densities. As λ increases, the kinetic contribution increases, which comes at the cost of a poorer density fit, as shown by the increase in $\Delta\rho_{L1}$. Meanwhile, the magnitude of the residual $|R|$ remains relatively stable across the range of λ values considered.

The right panel shows the impact of λ on v_{xc} near the nucleus. For higher λ values,

specifically 0.0002, 0.0005, and 0.001, an unphysical artifact in the potential is observed very close to the nucleus: the potential at the nucleus takes a higher value than expected, then decreases and reaches a minimum in the 0.02–0.05 bohr range, followed by the expected increase with distance.

As we move away from the nucleus, v_{xc} values across different λ values converge, with those in the λ range 0.00001 to 0.0002 being almost indistinguishable.

Considering the impact of λ on the potential close to the nucleus, and the consistency of potentials in the range 0.00001 to 0.0002, we selected $\lambda = 0.00005$ for He through O and $\lambda = 0.0001$ for F and Ne, for all calculations in this work. For F and Ne, using a higher λ helped in achieving lower residual norms and more accurate energy densities.

λ	$\Delta\rho_{L1}$	$ R $
0.00001	0.00101	0.00013
0.00002	0.00189	0.00014
0.00005	0.00424	0.00013
0.0001	0.00784	0.00008
0.0002	0.01443	0.00006
0.0005	0.03204	0.00006
0.001	0.05819	0.00008

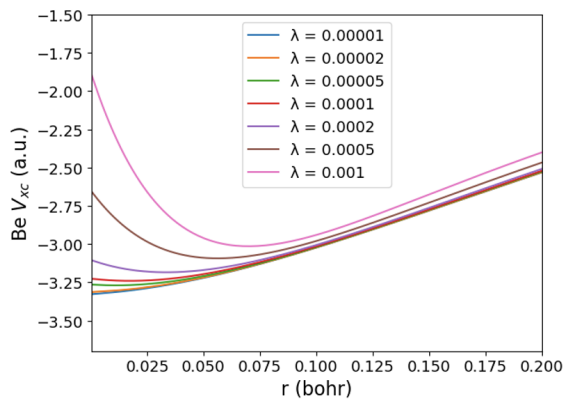


Figure S1: Impact of λ on the computed exchange-correlation potentials for Be.

S5. Comparison of the PBE orbital-averaged (OA) v_{xc} with the PBE functional derivative for Ne

The orbital-averaged exchange-correlation potential (OA v_{xc}) was computed for Ne using KS orbitals derived from the PBE⁵ density. The $\Delta\rho_{L1}$, which measures the difference between the PBE target density and the density obtained from the derived KS orbitals, was found to be 0.00037 per electron. Additionally, the magnitude of the residual $|R|$ per orbital was 0.00134.

As shown in Fig. S2, the OA v_{xc} agrees very well with the functional derivative of PBE⁵ across most regions of space. Close to the nucleus, where the functional derivative of PBE becomes unbounded, deviation between the two potentials is observed.

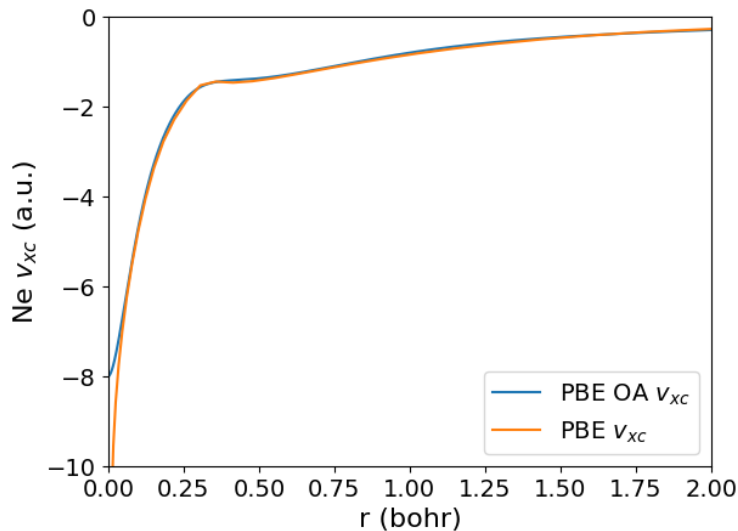


Figure S2: Comparison of the PBE orbital-averaged (OA) v_{xc} with the PBE functional derivative for Ne.

S6. Virial of the XC potential

The virial of the exchange-correlation potential is defined as:

$$t_{xc} = - \int \rho(\mathbf{r}) \mathbf{r} \cdot \nabla v_{xc}(\mathbf{r}) d\mathbf{r} \quad (1)$$

From virial relations,⁶ we know that for the exact exchange correlation potential,

$$E_{xc} + T_c = t_{xc}, \quad (2)$$

where $T_c = T - T_s$. This relation can be used to examine the accuracy of computed potentials, with deviations between the left and right side being indicative of errors in v_{xc} . For select atoms, we report virial t_{xc} , and $E_{xc} + T_c$ values in Table S2. Reasonable agreement between the two sides is seen, with the largest deviation being only 4.3 mHa for N.

Table S2: Comparison of the virial of v_{xc} and $E_{xc} + T_c$.

	He	Be	N
t_{xc} (Ha)	-1.0278	-2.6949	-6.5882
$E_{xc} + T_c$ (Ha)	-1.0278	-2.6940	-6.5925
% Difference	0.0000	0.0334	0.0652

S7. Quadratic Scaling of Total Ionization Energy

Figure S3 shows the total ionization energies for He through Ne plotted as a function of atomic number (Z). Ionization energy values for atoms and atomic ions were obtained from the NIST Atomic Spectra Database.⁷ The data is well described by a quadratic fit, given by: $1.76Z^2 - 5.54Z + 7.85$, with an $R^2 = 0.9997$.

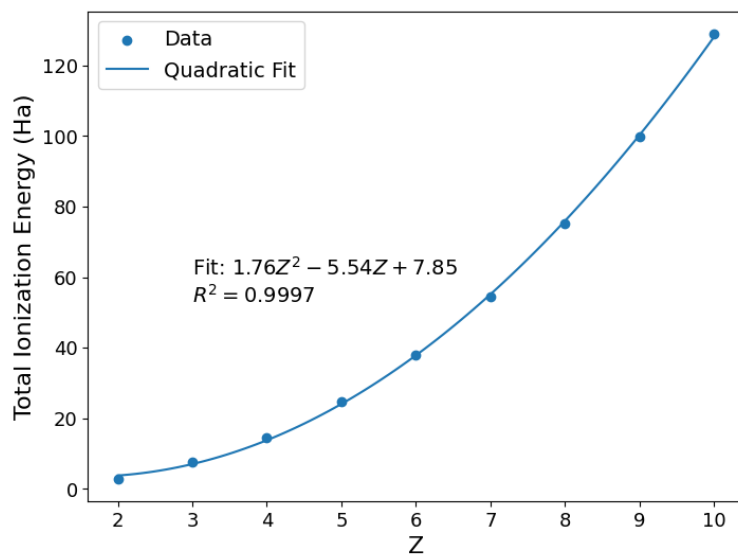


Figure S3: Total ionization energy vs. atomic number (Z) for He through Ne.

References

- (1) Kato, T. On the eigenfunctions of many-particle systems in quantum mechanics. *Comm. Pure Appl. Math.* **1957**, *10*, 151–177.
- (2) Handy, N. C. The molecular physics lecture 2004: (i) Density functional theory, (ii) Quantum Monte Carlo. *Mol. Phys.* **2004**, *102*, 2399–2409.
- (3) Tribedi, S.; Dang, D.-K.; Kanungo, B.; Gavini, V.; Zimmerman, P. M. Exchange correlation potentials from full configuration interaction in a Slater orbital basis. *J. Chem. Phys.* **2023**, *159*, 054106.
- (4) Rask, A. E.; Li, L.; Zimmerman, P. M. Kohn–Sham Density in a Slater Orbital Basis Set. *J. Phys. Chem. A* **2024**, *128*, 3194–3204.
- (5) Perdew, J. P.; Burke, K.; Ernzerhof, M. Generalized Gradient Approximation Made Simple. *Phys. Rev. Lett.* **1996**, *77*, 3865–3868.
- (6) Levy, M.; Perdew, J. P. Hellmann-Feynman, virial, and scaling requisites for the exact universal density functionals. Shape of the correlation potential and diamagnetic susceptibility for atoms. *Phys. Rev. A* **1985**, *32*, 2010–2021.
- (7) Kramida, A.; Ralchenko, Y.; Reader, J.; Team, N. A. NIST Atomic Spectra Database (version 5.12). <https://physics.nist.gov/asd>, 2024; National Institute of Standards and Technology, Gaithersburg, MD.